



Cite this: *Nanoscale*, 2025, **17**, 14887

## Layer-controlled continuous MoS<sub>2</sub> growth using a spin-coatable metal precursor buffer†

Dong Hwan Kim,<sup>‡</sup> Jinyoung Seo,<sup>‡</sup> Yoonbeen Kang,<sup>‡</sup> Bumjun Lee<sup>b</sup> and Sang-Yong Ju<sup>‡</sup> <sup>\*a,b</sup>

Continuous large-area MoS<sub>2</sub> growth holds significant potential for next-generation optoelectronic applications, yet achieving it efficiently and reproducibly with the conventional chemical vapor deposition (CVD) process remains a challenge due to inconsistent precursor adsorption and non-uniform nucleation. In this study, we developed a pH-optimized metal precursor buffer that enables uniform spin-coating and facilitates continuous MoS<sub>2</sub> growth. Sodium cholate (SC) acts as both a dispersant and a buffer, transforming molybdenum oxide into a dispersion-stable sodium molybdate (Na<sub>2</sub>MoO<sub>4</sub>)/SC complex. This complex forms a stable, uniformly spin-coatable dispersion at pH = 5.3, allowing it to form hydrogen bonds with the SiO<sub>2</sub>/Si substrate. Additionally, increasing the complex concentration enhances precursor adsorption, enabling controlled MoS<sub>2</sub> layer formation *via* CVD. Using this approach, we successfully fabricated continuous, centimeter-scale MoS<sub>2</sub> films in varying layer numbers. Real-time observation reveals the growth kinetics of the continuous MoS<sub>2</sub> film in terms of contrast value, according to the reaction time and temperature, indicating that the growth can occur at temperatures as low as 500 °C. This stable, scalable, and reproducible spin-coating technique, utilizing a metal precursor buffer, offers a robust pathway for producing large-area transition metal chalcogenide structures, advancing the development of 2D material-based applications.

Received 22nd March 2025,  
 Accepted 15th May 2025

DOI: 10.1039/d5nr01193k

[rsc.li/nanoscale](http://rsc.li/nanoscale)

## Introduction

Transition metal dichalcogenides (TMCs) possess unique optoelectronic properties<sup>1–4</sup> and tunabilities<sup>5–8</sup> essential for various advanced applications, including field-effect transistors,<sup>2,9–12</sup> spintronics,<sup>13–17</sup> and photocatalysis.<sup>18,19</sup> Achieving large-area, high-quality TMC structures necessitates precise and reproducible control over the growth process. Among the widely used techniques, chemical vapor deposition (CVD), which employs metal and chalcogen precursors,<sup>20–26</sup> plays a crucial role in facilitating controlled and scalable TMC growth.

Alkali halide molten salts<sup>22,24–29</sup> have been identified as rapid and reproducible catalysts for converting metal precursors into various TMCs *via* CVD growth. For example, Li *et al.*<sup>24</sup> demonstrated that sodium chloride promotes the growth of MoS<sub>2</sub> nanoribbons through the vapor–liquid–solid (VLS) mechanism. They also emphasized that alkali metals, rather

than halides, play a more crucial role in MoS<sub>2</sub> formation. A recent study using an integrated chemical vapor deposition microscope (ICVDM) revealed that sodium particles acted as catalysts, enhancing growth by scooting along MoS<sub>2</sub> grain edges and facilitating MoS<sub>2</sub> laminate precipitation.<sup>26</sup> Consequently, sodium<sup>22,25–27,29</sup> plays a pivotal role in the growth process, and controlling its activity presents a potential strategy for achieving large-area, high-quality TMC growth.

Among various molybdenum precursors, molybdenum oxide (MoO<sub>3</sub>) and sodium molybdate (Na<sub>2</sub>MoO<sub>4</sub>) are widely used for MoS<sub>2</sub> growth. In the CVD process, MoO<sub>3</sub> is typically sublimed from a crucible onto a target substrate to form MoS<sub>2</sub>,<sup>20,21,30,31</sup> while Na<sub>2</sub>MoO<sub>4</sub> is directly coated onto the substrate as a metal precursor.<sup>25,29</sup> Notably, Na<sub>2</sub>MoO<sub>4</sub> contains sodium catalyzing the MoS<sub>2</sub> growth.<sup>25</sup> Recently, Li *et al.*<sup>25</sup> reported that whereas a continuous MoS<sub>2</sub> film has been successfully grown on a sapphire substrate using Na<sub>2</sub>MoO<sub>4</sub>, achieving the same on SiO<sub>2</sub>/Si substrates remains challenging. This infers that surface charges on both the metal precursor and the substrate play a crucial role in precursor adsorption and the formation of a continuous MoS<sub>2</sub> film.

In this study, we successfully achieved continuous centimeter-scale polycrystalline MoS<sub>2</sub> growth using a spin-coatable metal precursor buffer *via* the CVD method. Sodium cholate (SC), serving as both a dispersant and a buffer, converts

<sup>a</sup>Graduate Program of Semiconductor Science and Engineering, Yonsei University, Seoul 03722, Republic of Korea. E-mail: [syju@yonsei.ac.kr](mailto:syju@yonsei.ac.kr)

<sup>b</sup>Department of Chemistry, Yonsei University, Seoul 03722, Republic of Korea

†Electronic supplementary information (ESI) available. See DOI: <https://doi.org/10.1039/d5nr01193k>

‡These authors contributed equally to this work.



layered MoO<sub>3</sub> into a monomeric Na<sub>2</sub>MoO<sub>4</sub>/SC complex upon sonication, enabling uniform spin-coating on O<sub>2</sub>-plasma-treated SiO<sub>2</sub> substrates. Additionally, the uniform spin-coating of metal precursors allows precise control over the number of MoS<sub>2</sub> layers across large areas, depending on the metal precursor concentration. The polycrystalline nature of the MoS<sub>2</sub> film was confirmed through transmission electron microscopy (TEM). Real-time observation of continuous MoS<sub>2</sub> formation provided insights into the growth pathway, as well as the relationship between temperature and time. Furthermore, the spin-coatable precursor demonstrated facile patterning capability, highlighting its potential for integration with other devices.

## Experimental

### Materials and instrumentation

Molybdenum(vi) oxide (purity ≥99.5%), sodium molybdate dihydrate (purity ≥99%), and sulfur (purity ≥99.5%) were procured from Merck. SC (purity ≥98%, TCI) was used as is. Deionized (DI) water with resistivity exceeding 18 MΩ cm was used to prepare the Na<sub>2</sub>MoO<sub>4</sub>/SC dispersion. Argon gas, with a purity greater than 99.99%, was supplied by Donga Gas and used as the CVD carrier gas. The Si wafer (285 nm thick SiO<sub>2</sub>/Si substrate, ShinEtsu) was cut into 1 × 1 cm<sup>2</sup> pieces, cleaned with methanol, acetone, and isopropanol, and dried using a nitrogen stream. The pH of the dispersions was measured with a SevenMulti pH meter (Mettler Toledo), calibrated with three known pH buffer references (*i.e.*, 4.01, 7.00, and 10.01). The zeta (ζ)-potential was determined in a quartz cuvette using an ELS-1000ZS (Otsuka Electronics) following standard procedures.<sup>32</sup> UV-vis absorption spectra were measured using a V-770 spectrophotometer (JASCO) with 1 mm path length cuvettes (21/Q/1, Starna Scientific), and extinction was recorded in a double-beam configuration. Atomic force microscopy (AFM) height images were obtained in tapping mode using an NX10 AFM (Park Systems), with Al-coated silicon cantilevers (force constant: 37 N m<sup>-1</sup>, resonance frequency: 300 kHz, ACTA-20, App Nano).<sup>33</sup> Images were captured at 512 × 512 pixels at a scan speed of 0.2 Hz. Topography flattening was performed using the XEI program (Park Systems) with a polynomial fit along the fast scan axis. Raman measurements in a back-scattering configuration were conducted using either a custom-built Raman system<sup>34,35</sup> or the XperRam C (Nanobase) with 532 nm excitation unless noted otherwise. To prevent sample damage, the laser power was kept below 0.1 mW. Optical images were captured with an upright fluorescence microscope (BX-51, Olympus) equipped with a CMOS camera (3.4 μm per pixel, 2560 × 1920 pixels). Water contact angles were measured with a contact angle goniometer (Phoenix 10, Surface Electro Optics) based on previous work.<sup>36</sup> X-ray photoelectron spectroscopy (XPS) data were acquired with K-alpha (Thermo Scientific), according to the literature.<sup>37</sup> A monochromatic X-ray source (Al K<sub>α</sub>: 1486.6 eV) with a beam size of 400 μm was used with a power of 12 kV and 3 mA under vacuum (sample pressure: 4.8 × 10<sup>-9</sup> mbar, base pressure: 2.9 × 10<sup>-9</sup> mbar). Ag

3d<sub>5/2</sub> was used as a charging reference for all samples. Survey scans were acquired with 200 eV pass energy at a step size of 1 eV. Detailed scans were obtained at 40 eV pass energy with a step size of 0.1 eV. The acquired spectra were baseline-subtracted using the Shirley profile. The C 1s peak (284.8 eV) from adventitious carbon was used as an internal reference. SC, MoO<sub>3</sub>, and Na<sub>2</sub>MoO<sub>4</sub> were used in their as-received powder forms. A Na<sub>2</sub>MoO<sub>4</sub>/SC dispersion was drop-cast onto a 285 nm thick SiO<sub>2</sub>/Si substrate, while MoS<sub>2</sub>, grown on a 285 nm thick SiO<sub>2</sub>/Si substrate, was cleaned with isopropanol prior to use. Peak fitting employs a Shirley-type background. The S 2p (Mo 3d) spin-orbit doublet separation was held constant at 1.2 (3.1) eV and with a 2 : 1 (3 : 2) area ratio.

### Surface hydrophilization (step i)

O<sub>2</sub>-plasma reactive ion etching (RIE, PS-100, Plasol) or inductively coupled plasma (ICP-RIE, IPS-5000, Sntec) was employed to hydrophilize a 285 nm thick SiO<sub>2</sub>/Si substrate and remove surface contaminants. The hydrophilization process typically involves applying the plasma at 100 W for 7 min. ICP-RIE treatment was conducted at 50 W for 40 s in the presence of O<sub>2</sub>/CF<sub>4</sub> flow with 25 sccm/25 sccm. Spin-coating of the metal precursor dispersion and subsequent steps were performed immediately after the O<sub>2</sub>-plasma or RIE treatment by minimizing exposure to ambient water.<sup>38</sup>

### Metal precursor preparation (step ii)

**Na<sub>2</sub>MoO<sub>4</sub>/SC dispersion preparation.** Following established protocols,<sup>26,30,31</sup> a dispersion was prepared by adding 20 mM MoO<sub>3</sub> to 1 wt% SC in 35 mL of DI water. This mixture underwent 1 h bath sonication, 2 h probe sonication, and 1 h centrifugation at 5000g ( $g = 9.8 \text{ m s}^{-2}$ ), with approximately 80% of the supernatant being collected. The dispersion was then filtered using a 0.2 μm PTFE syringe filter. The final pH of the dispersion is ~5.3. The decreased or increased pH of the dispersions was attained using smaller amounts of SC or sodium hydroxide solution, respectively. The filtered Na<sub>2</sub>MoO<sub>4</sub>/SC dispersion was placed on the substrate and spin-coated at 5000 rpm for 1 min. Similar procedures were followed to prepare a 20 mM MoO<sub>3</sub> dispersion without SC, a 20 mM Na<sub>2</sub>MoO<sub>4</sub> dispersion without SC, and a 20 mM MoO<sub>3</sub> dispersion containing 1 wt% sodium dodecylsulfate (SDS). These stock samples were diluted for experimental use.

### MoS<sub>2</sub> growth (step iii)

All CVD growths were carried out using an ICVDM.<sup>26</sup> **MoS<sub>2</sub> growth:** prior to CVD growth, the 285 nm thick SiO<sub>2</sub>/Si substrate was treated with O<sub>2</sub> plasma. Immediately afterward, 100 μL of the Na<sub>2</sub>MoO<sub>4</sub>/SC dispersion was spin-coated at 5000 rpm for 1 min on an O<sub>2</sub> plasma-treated substrate, which was then placed in a mini-CVD crucible. In a separate alumina crucible, 1000 mg of sulfur was loaded into the sulfur tube furnace. Parameters for the mini-CVD, charge-coupled device (CCD), chalcogen tube furnace, and flow controller were set accordingly.  $T_{\text{CVD}}$  and  $T_{\text{S}}$  were ramped to 750 °C and 250 °C, respectively, with an  $F_{\text{Ar}} = 180$  sccm argon flow. The growth temperature was maintained for 20 min, reached by ramping



the temperatures at rates of  $42\text{ }^{\circ}\text{C min}^{-1}$  for sulfur and  $100\text{ }^{\circ}\text{C min}^{-1}$  for the spin-coated sample. After the growth, the system was allowed to naturally cool to room temperature. Real-time images were captured using a long working-distance  $50\times$  objective lens (LMPlanFL, working distance: 10.6 mm, N.A.: 0.50, Olympus). A Retiga R6 CCD (Teledyne) was used to collect image stacks, which were then analyzed using the Fiji program. These images were compared with a video containing real-time parameters such as  $t_{\text{rxn}}$ ,  $T_{\text{CVD}}$ ,  $T_{\text{S}}$ , and  $F_{\text{Ar}}$ . **Patterned TMC growth:** a metal mask was used to create a cross-shaped hydrophilic pattern on the substrate *via* RIE exposure. Immediately after, the sample was spin-coated with a 6 mM  $\text{Na}_2\text{MoO}_4/\text{SC}$  dispersion and subjected to CVD growth. **Sodium particle removal:**  $\text{MoS}_2$  samples were immersed in toluene for 20 min to remove non-covalent sulfur and then dried using nitrogen gas. The samples were subsequently treated with isopropanol to remove sodium until no gas was generated from the surface.  $C_{\text{R}}$  was obtained using the following equation:  $C_{\text{R}} = (R_{\text{S}} - R_0)/R_0$ , where  $R_{\text{S}}$  and  $R_0$  denote the reflection intensities of the  $\text{MoS}_2$  sample on a substrate and bare substrate, respectively.

### TEM measurements

**Sample preparation.** Sample transfer and measurements followed established protocols.<sup>26,39</sup> Poly(methyl methacrylate) (PMMA) (A2, M.W.: 950 kDa) was used for transferring the sample to a TEM grid with lacey carbon. The underlying  $\text{SiO}_2/\text{Si}$  substrate was etched using a buffered oxide etchant (10 : 1 volume ratio of 36%  $\text{NH}_4\text{F}$  and 4.7% HF,  $1\text{ nm s}^{-1}$  etching rate at  $25\text{ }^{\circ}\text{C}$ , Merck). The sample was then picked up with a TEM grid, and PMMA was dissolved in acetone. The transferred sample was annealed at  $300\text{ }^{\circ}\text{C}$  under 17 mTorr for 1 h using a tube furnace. TEM images were obtained using an aberration-corrected TEM (JEM-ARM 200F Neoarm, Jeol) at 200 kV. HAADF-STEM images were collected at 80 kV after stabilization with TEM accessories, using an aberration-corrected NEOASCOR high-order aberration corrector. **Polycrystallinity analysis:** Gatan software was utilized to analyze polycrystallinity. The FFT of each TEM image was obtained, and TEM images from specific hexagonal diffraction patterns were gen-

erated to indicate each domain. These images were then overlapped to create composite domain-specific TEM images.

## Results and discussion

### Effects of $\text{pK}_{\text{a}}$ on uniform spin-coating of the precursor dispersion

We hypothesize that the surface charge of the metal precursor plays a crucial role in interacting with the surface charge of the  $\text{SiO}_2/\text{Si}$  substrate, thereby influencing uniform coating on the substrate. A transparent  $\text{Na}_2\text{MoO}_4$  solution, in which  $\text{Na}_2\text{MoO}_4$  is highly soluble in water, exhibits basic pH.<sup>40</sup> Considering the reported  $\text{pK}_{\text{a}}$  values of silanol on  $\text{SiO}_2$  (*i.e.*, 9.8)<sup>41</sup> and alumina on sapphire (*i.e.*, 12.2),<sup>25</sup> a basic  $\text{Na}_2\text{MoO}_4$  solution would create anionic repulsion with silanol moieties on the  $\text{SiO}_2/\text{Si}$  substrate, leading to poor adsorption. Therefore, achieving reproducible and continuous  $\text{MoS}_2$  growth requires a buffered  $\text{Na}_2\text{MoO}_4$  solution with mildly acidic pH. To address this, SC functions as both a dispersant and a buffer, converting  $\text{MoO}_3$  into an  $\text{Na}_2\text{MoO}_4/\text{SC}$  complex.  $\text{MoO}_3$  was chosen over  $\text{Na}_2\text{MoO}_4$  to prevent the formation of sodium chloride during pH adjustment, as sodium chloride has been reported to promote  $\text{MoS}_2$  nanoribbon growth.<sup>24</sup>

Fig. 1 presents a schematic representation of the process for creating a continuous  $\text{MoS}_2$  film from the spin-coatable metal precursor buffer *via* CVD growth (see the Experimental section). The process begins with hydrophilizing a 285 nm thick  $\text{SiO}_2/\text{Si}$  substrate through  $\text{O}_2$ -plasma treatment (step i), a crucial step for ensuring uniform spin-coating of the metal precursor dispersion and facilitating subsequent  $\text{MoS}_2$  growth. Immediately afterward, while minimizing exposure to moisture, the pH-controlled metal precursor dispersion is spin-coated onto the hydrophilized substrate (step ii). This precursor-coated sample is then subjected to CVD growth at  $750\text{ }^{\circ}\text{C}$  for 20 min using sulfur and argon gases, converting the precursor into a  $\text{MoS}_2$  film (step iii). During step ii, moisture can disrupt hydrogen bonding between the spin-coated metal precursor and the hydrophilic substrate, thereby leading to non-uniform adsorption of the metal precursor.

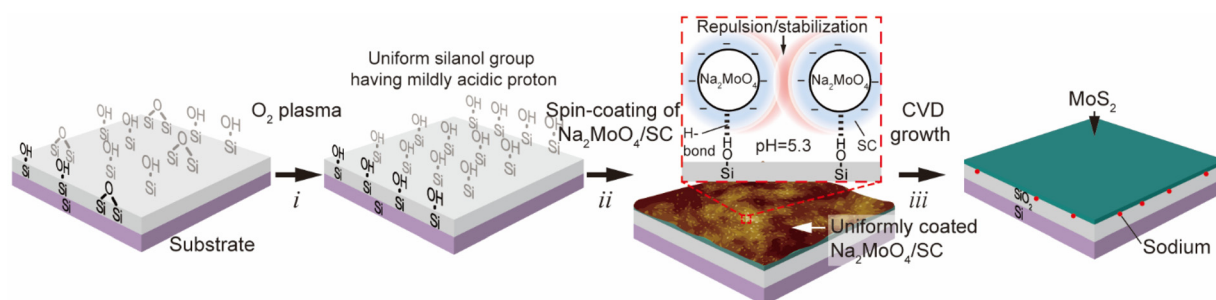


**Fig. 1** Schematic of continuous large-area  $\text{MoS}_2$  growth using spin-coatable pH-controlled SC-buffered metal precursor dispersion. Surface hydrophilization (i): enhancing the  $\text{SiO}_2/\text{Si}$  substrate's hydrophilicity *via*  $\text{O}_2$  plasma treatment. Precursor spin-coating (ii): depositing a uniform layer of a buffered  $\text{Na}_2\text{MoO}_4/\text{SC}$  dispersion through spin-coating. Inset: illustration of repulsive  $\text{Na}_2\text{MoO}_4/\text{SC}$  particles forming hydrogen bonds with silanol groups on the substrate.  $\text{MoS}_2$  growth (iii): converting the spin-coated precursor into  $\text{MoS}_2$  *via* CVD sulfurization, followed by isopropanol washing.



This method involves the sonication of  $\text{MoO}_3/\text{SC}$  in DI water.  $\text{MoO}_3$ , which appears yellowish, has an orthorhombic structure<sup>42</sup> where edge-sharing octahedra form chains that are cross-linked by oxygen atoms to create layered structures. Sonication disrupts these cross-linked layers, leading to the formation of sodium molybdate. During this process, slightly water-soluble  $\text{MoO}_3$  hydrates and converts into molybdic acid ( $\text{H}_2\text{MoO}_4$ ).<sup>43</sup> Molybdic acid, a polyprotic acid with closely spaced  $\text{pK}_a$  values ( $\text{pK}_{a1} = 3.61\text{--}4.0$  and  $\text{pK}_{a2} = 3.89\text{--}4.37$ ),<sup>44–46</sup> transitions into sodium molybdate upon reaction with sodium cations. SC, which acts as both an adhesion promoter<sup>23</sup> and a dispersant,<sup>26</sup> has a  $\text{pK}_a$  value of approximately 5.3,<sup>47</sup> enabling it to function as a buffer under mildly acidic conditions. Near neutral pH, the metal acid undergoes ion exchange with SC, forming water-soluble sodium molybdate and water-insoluble cholic acid. Additionally, as illustrated in step ii, the silanol ( $\text{Si-OH}$ ) groups on a hydrophilized  $\text{SiO}_2/\text{Si}$  substrate have a  $\text{pK}_a$  value of around 9.8.<sup>41</sup> Under mildly acidic conditions, these silanol groups form strong hydrogen bonds with sodium molybdate and SC (e.g.,  $\text{Si-OH}\cdots\text{O}=\text{Mo}$  and  $\text{Si-OH}\cdots\text{O}=\text{C}$ ), while the metal precursors repel each other, promoting uniform dispersion.

The metal precursor dispersion was prepared by sonication of a 20 mM  $\text{MoO}_3$  solution with 1 wt% SC in DI water, forming

an *in situ* sodium molybdate/SC complex with a pH below 7. Following sonication and centrifugation, the dispersion exhibited a pH of approximately 5.3. To create dispersions with varying pH levels, lesser amounts of SC or sodium hydroxide were used instead of hydrochloric acid, as the latter would generate  $\text{NaCl}$ , which can promote  $\text{MoS}_2$  nanoribbon formation.<sup>24</sup>

The surface charges of these dispersions were analyzed using  $\zeta$ -potential measurements, as shown in Fig. 2a. Dispersions at pH 4.2 and 5.3 show a shoulder peak at  $-8.3$  mV and bimodal peaks at  $-9.5/-58.7$  mV, respectively. In contrast, dispersions at pH 2.4, 10.3, and 12.8 displayed peaks ranging from  $-0.26$  to  $-2.1$  mV. These findings suggest the presence of two distinct components: one whose surface charge varies with pH and another whose charge remains mostly unchanged. The pH 5.3 dispersion contains both anionic  $\text{Na}_2\text{MoO}_4/\text{SC}$ , corresponding to the  $-58.7$  mV peak, and nearly undispersed layered  $\text{MoO}_3$  with SC, corresponding to the  $-9.5$  mV peak. Additionally, a significant portion of the dispersion exhibited  $\zeta$ -potential values below  $-10$  mV, presumably attributed to the few terminal hydroxy groups of partially broken layered  $\text{MoO}_3$ , indicating an unstable dispersion. This result confirms that SC facilitates the *in situ* formation of  $\text{Na}_2\text{MoO}_4/\text{SC}$  due to its buffering capability in the pH range of

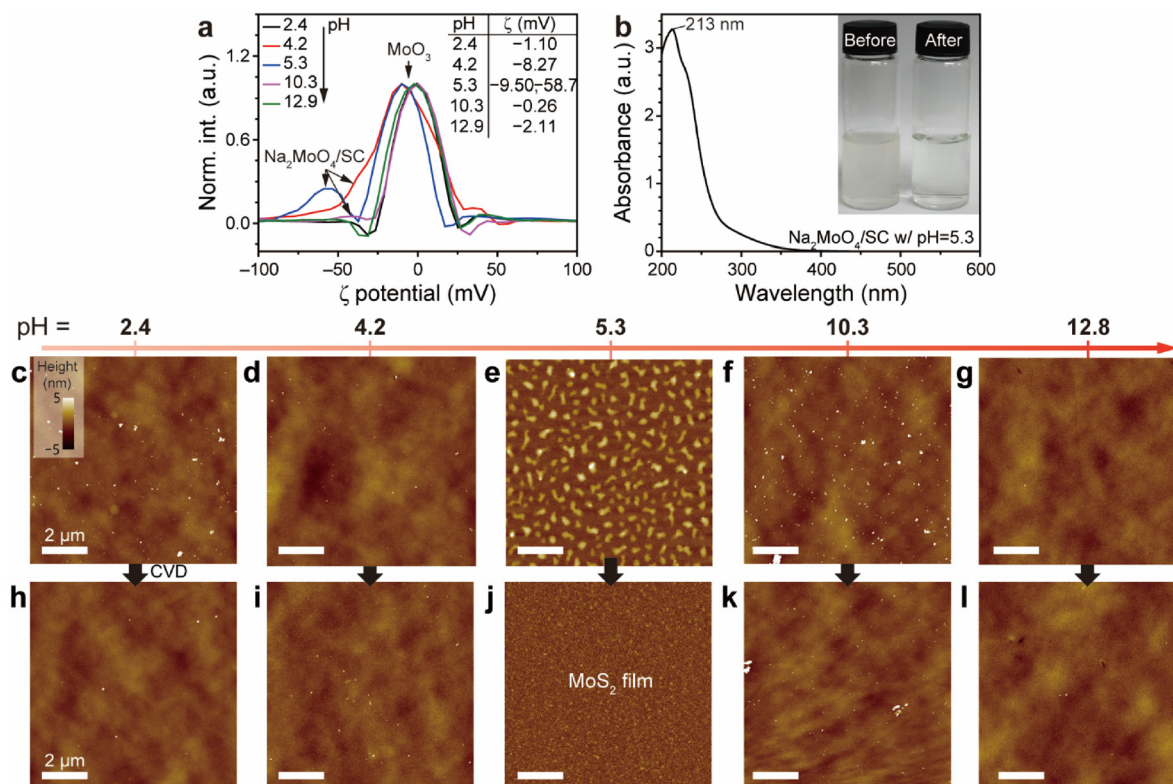


**Fig. 2** Impact of pH on spin-coated  $\text{MoO}_3/\text{SC}$  adsorbates and subsequent  $\text{MoS}_2$  formation. (a)  $\zeta$ -Potential measurements of  $\text{MoO}_3/\text{SC}$  dispersions at varying pH levels (i.e., 2.4, 4.2, 5.3, 10.3, and 12.8). (b) The absorption spectrum of the filtered aqueous  $\text{Na}_2\text{MoO}_4/\text{SC}$  stock dispersion (black). Inset: photographs of before and after 0.2  $\mu\text{m}$  filtration of the  $\text{Na}_2\text{MoO}_4/\text{SC}$  dispersion. (c–g) AFM topography images of  $\text{Na}_2\text{MoO}_4/\text{SC}$  spin-coated films at pH values of (c) 2.4, (d) 4.2, (e) 5.3, (f) 10.3, and (g) 12.8, with consistent height scales and scale bars. (h–l) The corresponding AFM images of the resulting  $\text{MoS}_2$  films grown *via* CVD sulfurization from each pH-controlled spin-coat.



4–6.<sup>32</sup> At higher pH levels, SC loses its buffer ability, and its fully anionic charge cannot stabilize  $\text{Na}_2\text{MoO}_4$  due to electrostatic repulsion, leaving only  $\text{MoO}_3$ . Based on these findings, we used the filtered complex dispersion at pH 5.3 for the rest of this study, referring to it as  $\text{Na}_2\text{MoO}_4/\text{SC}$  unless otherwise specified.

The inset of Fig. 2b shows a photograph of before and after the 0.2  $\mu\text{m}$  filtration of the  $\text{Na}_2\text{MoO}_4/\text{SC}$  dispersion. The filtered sample is devoid of turbidity originating from  $\text{MoO}_3$ . Fig. 2b displays the absorption spectrum of the filtered  $\text{Na}_2\text{MoO}_4/\text{SC}$  dispersion with pH  $\sim 5.3$ . The  $\text{Na}_2\text{MoO}_4/\text{SC}$  dispersion exhibits a peak at 213 nm. The absorption bands between 200 and 400 nm correspond to ligand-to-metal charge transfer transitions ( $\text{O}^{2-} \rightarrow \text{Mo}^{6+}$ ),<sup>48</sup> and the spectral shape aligns with that of  $\text{Na}_2\text{MoO}_4$ ,<sup>49</sup> in contrast to the broad visible-range absorption typically seen with  $\text{MoO}_3$ .

AFM results of pH-controlled metal precursors and subsequent films support the  $\text{pK}_a$  hypothesis. We investigated samples at various pH values (2.4, 4.2, 5.3, 10.3, and 12.8), taking into account the  $\text{pK}_a$  values of molybdic acid, SC, and silanol moieties. The dispersions were spin-coated on the freshly  $\text{O}_2$ -treated 285 nm thick  $\text{SiO}_2/\text{Si}$  substrate while minimizing exposure to the atmosphere. Without the treatment, the sample failed to form a uniform  $\text{MoS}_2$  film despite both samples exhibiting similar surface morphologies and average surface roughness values ( $\langle R \rangle \approx 0.2$  nm) (see detailed characterization and a full explanation in Fig. S1a–S1g and Note S1†). Fig. 2c–g display AFM height images of the spin-coated  $\text{Na}_2\text{MoO}_4/\text{SC}$  dispersions at different pH levels. Notably, the spin-coat at pH 5.3 displays dense elongated droplet-like features with uniform height, whereas those at other pH levels display sporadic particle aggregates. This result correlates with the relative stability of the  $\text{Na}_2\text{MoO}_4/\text{SC}$  complex observed in the  $\zeta$ -potential measurements. These findings align with the  $\text{pK}_a$  hypothesis, where the mildly acidic dispersion (pH = 5.3) facilitates multiple hydrogen bonds with silanol groups while causing repulsion between metal precursors.

A similar trend is observed in the CVD-grown samples. CVD growth results in different films based on pH. Fig. 2h–l show AFM images of  $\text{MoS}_2$  films grown from dispersions at various pH values. Samples from pH 2.4, 4.2, 10.3, and 12.8 exhibit sporadic particle aggregates, while that from pH 5.3 yields a continuous  $\text{MoS}_2$  film from the previously discontinuous adsorbates, indicating  $\text{MoS}_2$  growth. As a result, the  $\text{Na}_2\text{MoO}_4/\text{SC}$  dispersion at pH 5.3 is used for further experiments. This control experiment demonstrates the effectiveness of the pH-controlled  $\text{Na}_2\text{MoO}_4/\text{SC}$  dispersion in achieving the formation of a continuous  $\text{MoS}_2$  film.

The transformation of organic dispersants, such as SC, during the growth process remains a subject of interest. Previous studies using *in situ* Raman spectroscopy and TEM coupled with energy-dispersive X-ray spectroscopy (EDS) have shown that amorphous carbon originating from SC begins to decompose around 500 °C.<sup>26</sup> This decomposition is also likely linked to the sulfurization of  $\text{Na}_2\text{MoO}_4$ , which, during its conversion to  $\text{MoS}_2$ , creates an *in situ* oxidative environment that

promotes the breakdown of SC and removal of SC-derived amorphous carbon. Additionally, TEM-EDS analysis detected no remaining traces of amorphous carbon.<sup>26</sup>

### Effect of precursor concentrations on $\text{MoS}_2$ films

The reproducible and uniform spin-coating capability of the  $\text{Na}_2\text{MoO}_4/\text{SC}$  complex on a hydrophilic  $\text{SiO}_2/\text{Si}$  substrate allowed for a quantitative study on the impact of the precursor concentration on the  $\text{MoS}_2$  film quality and layer number. To explore this, the 20 mM  $\text{Na}_2\text{MoO}_4/\text{SC}$  stock dispersion was diluted, and the corresponding  $\text{MoS}_2$  films were then prepared *via* the CVD process. Fig. 3a–d show AFM height images of spin-coated  $\text{Na}_2\text{MoO}_4/\text{SC}$  at different concentrations. The 4 mM sample does not exhibit any distinct features, and closely resembles the native morphology of the 285 nm thick  $\text{SiO}_2/\text{Si}$  substrate (Fig. S1c†). However, samples at 6 mM and higher show noticeably elongated adsorbates with increasing heights and sizes. Height profiles in Fig. S2a† indicate that  $\text{Na}_2\text{MoO}_4/\text{SC}$  adsorbates reach heights up to 7 nm. Quantitative analysis (Fig. S2b†) reveals that as  $\text{Na}_2\text{MoO}_4/\text{SC}$  concentrations increase, the adsorbate density decreases, while the volume ( $V$ ) of each individual adsorbate increases. This suggests that dilution can control the concentration of the precursor adsorbate on the substrate.

Fig. 3e–h show AFM topographies of the corresponding  $\text{MoS}_2$  films formed by CVD sulfurization of each sample followed by isopropanol washing. The  $\text{MoS}_2$  films are continuous across all samples. Upon closer inspection, varying heights are observed beneath the  $\text{MoS}_2$  films, as shown in Fig. S2c.† Since the samples were grown with a sodium catalyst, sodium is likely present underneath the  $\text{MoS}_2$  films, which is in line with the literature.<sup>50</sup> After thoroughly washing the  $\text{MoS}_2$  surface with isopropanol to remove surface sodium, EDS (Fig. S3a–S3d†) confirms the presence of sodium underneath. Sodium is randomly distributed across the surface. Atomic composition analysis (Fig. S3e†) shows that the atomic percentages of Na, Mo, and S are 11.9, 40.4, and 47.7%, respectively. This result suggests that the  $\text{MoS}_2$  film not only contains sodium underneath the surface but also exhibits an imbalanced Mo/S stoichiometry, in line with the literature.<sup>25</sup>

XPS measurements show the chemical states of the elements present. Fig. S4a–S4d† display the survey and detailed spectra of S 2p, Mo 3d, and Na 1s (see Note S2† for a detailed explanation). In the S 2p region (Fig. S4b†), only the  $\text{MoS}_2$  film exhibits the characteristic spin-orbit doublet peaks —S 2p<sub>3/2</sub> at 161.1 eV and S 2p<sub>1/2</sub> at 162.2 eV—indicative of metal sulfide.<sup>37</sup> Similarly, in the Mo 3d region (Fig. S4c†), only the  $\text{MoS}_2$  film shows the  $\text{Mo}^{4+}$  spin-orbit doublet, with 3d<sub>5/2</sub> at 228.2 eV and 3d<sub>3/2</sub> at 231.3 eV (3.1 eV separation), whereas the  $\text{MoO}_3$ ,  $\text{Na}_2\text{MoO}_4$ , and  $\text{Na}_2\text{MoO}_4/\text{SC}$  drop-cast samples display features corresponding to  $\text{Mo}(vi)$ . In the Na 1s region (Fig. S4d†), the  $\text{MoS}_2$  film shows a neutral sodium signal at 1071.4 eV, while the other samples show red-shifted singlet peaks between 1070.2 and 1070.7 eV, consistent with the presence of neutral amorphous sodium as confirmed by TEM images and sodium diffraction patterns.<sup>26</sup> Additionally, the



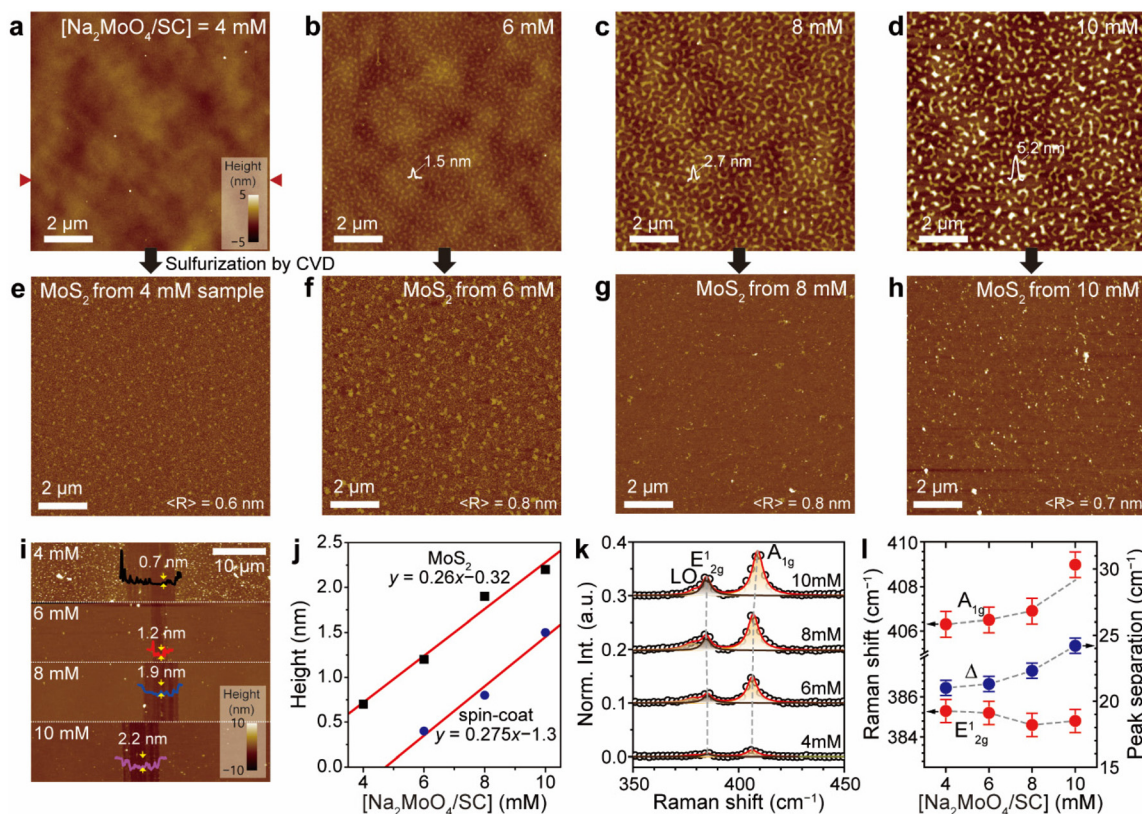


**Fig. 3** Systematic changes in precursor and MoS<sub>2</sub> morphologies with increasing Na<sub>2</sub>MoO<sub>4</sub>/SC concentrations. (a–d) AFM height images of adsorbates from spin-coated Na<sub>2</sub>MoO<sub>4</sub>/SC dispersions at concentrations of 4, 6, 8, and 10 mM. (e–h) The corresponding MoS<sub>2</sub> films formed by CVD sulfuration of each spin-coated sample through the CVD process. (i) Composite AFM height image composed of four scratched MoS<sub>2</sub> quarters, each representing a different Na<sub>2</sub>MoO<sub>4</sub>/SC concentration. (j) Average height profile trends of the spin-coats and the corresponding MoS<sub>2</sub> films. Red lines denote linear regression fits. (k) Normalized Raman spectra of MoS<sub>2</sub> samples, with an Si band at 520.9 cm<sup>-1</sup> as a reference, at various Na<sub>2</sub>MoO<sub>4</sub>/SC concentrations. (l) Plot showing the positions and peak separations of E<sub>12g</sub><sup>1</sup> and A<sub>1g</sub> bands of MoS<sub>2</sub> samples as a function of Na<sub>2</sub>MoO<sub>4</sub>/SC concentration.

drop-cast sample shows a blue-shifted peak at 1070.7 eV compared to the Na<sub>2</sub>MoO<sub>4</sub> powder (1070.2 eV), which qualitatively aligns with observations from the spin-coated Na<sub>2</sub>MoO<sub>4</sub>.<sup>50</sup>

Fig. 3i presents a composite AFM height image composed of four scratched MoS<sub>2</sub> film quarters from each concentration, showing step heights of approximately 0.7, 1.2, 1.9, and 2.2 nm. These correspond to near single-layer (SL), bi-layer (BL), tri-layer (TL), and multi-layer (ML) MoS<sub>2</sub>. A comparison of height trends (Fig. 3j) reveals a linear correlation between the average thicknesses of the spin-coated precursor layers and the resulting MoS<sub>2</sub> films. The spin-coat thickness  $y_{\text{spincoat}}$  varies linearly with concentration as  $y_{\text{spincoat}} = 0.275x - 1.3$ , where  $x$  is the Na<sub>2</sub>MoO<sub>4</sub>/SC concentration. Similarly, the MoS<sub>2</sub> film thickness  $y_{\text{MoS}_2}$  follows the relation  $y_{\text{MoS}_2} = 0.26x - 0.32$ . Combining these two expressions yields a direct correlation between the precursor layer and the film thickness as follows:

$$y_{\text{MoS}_2} = 0.945y_{\text{spincoat}} - 0.91 \text{ nm} \quad (1)$$

This empirical eqn (1) provides a practical thickness conversion factor, useful for estimating and targeting the desired MoS<sub>2</sub> film thickness.

Raman spectra of the MoS<sub>2</sub> films, as shown in Fig. 3k, reveal systematic changes in the E<sub>12g</sub><sup>1</sup> and A<sub>1g</sub> bands with increasing Na<sub>2</sub>MoO<sub>4</sub>/SC concentrations. The interpeak separation and their intensities progressively increase as Na<sub>2</sub>MoO<sub>4</sub>/SC concentrations rise. The interpeak separation (Fig. 3l) for the 4 mM-derived sample shows 21.0 cm<sup>-1</sup>, while samples from 6 mM and higher show an increase in separation, reaching up to 24.2 cm<sup>-1</sup>, indicating a transition from BL to ML MoS<sub>2</sub>,<sup>32,51</sup> in line with AFM results. This result demonstrates the ability to control the number of MoS<sub>2</sub> layers by adjusting the precursor concentration.

This method enables the growth of continuous, large-area MoS<sub>2</sub> films on a centimeter scale. Fig. 4a shows photographs of the fully grown continuous MoS<sub>2</sub> on a 285 nm thick SiO<sub>2</sub>/Si substrate, both with and without masking. The left image shows the film without masking, while the right one shows the masked area, created using Denko tape during the spin-coating process to generate different contrasts in the exposed regions. The uniformity of the MoS<sub>2</sub> film was confirmed by point Raman spectra taken across the sample. Raman spectra (Fig. 4b) exhibited consistent positions (*i.e.*, ~383.8 and ~404.2 cm<sup>-1</sup>), interpeak separation (~20.4 cm<sup>-1</sup>), and intensi-



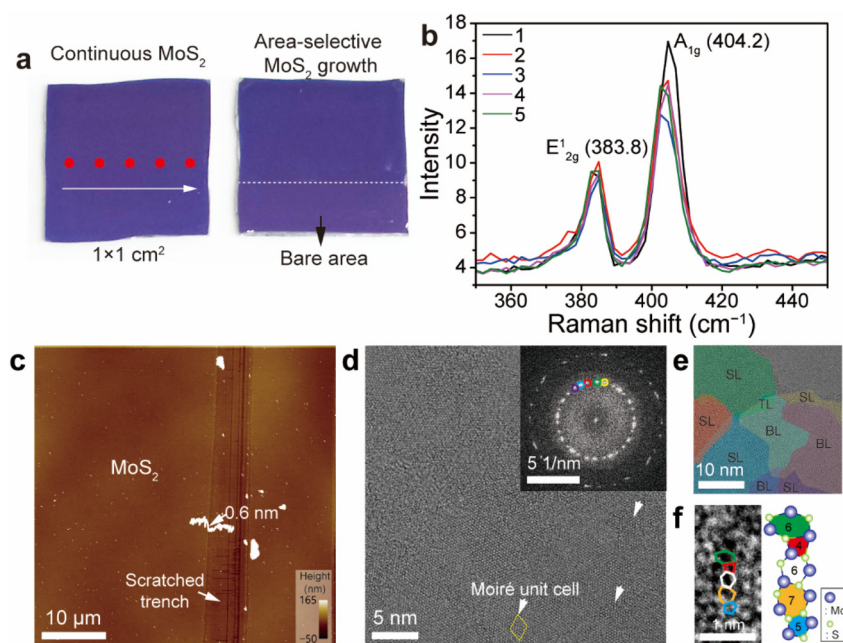


**Fig. 4** Continuous large-area polycrystalline FL MoS<sub>2</sub>. (a) Continuous large-area MoS<sub>2</sub> (left) and continuous large-area MoS<sub>2</sub> with a bare area generated using Denko tape during the spin-coating process (right). (b) Raman spectra taken across the entire MoS<sub>2</sub> sample as indicated in (a). (c) AFM image of a scratched MoS<sub>2</sub> film. (d) HAADF-STEM image of the polycrystalline MoS<sub>2</sub> film showing sporadic Moiré patterns marked by white arrows. Inset: diffraction patterns displaying five distinct sets of hexagonal patterns. (e) Color-coded representation of MoS<sub>2</sub> polycrystallites based on five crystal orientations, highlighting BL and TL regions with distinct Moiré patterns, as well as SL regions. (f) HAADF-STEM image showing grain boundaries with lined (6|4)–(7|5) defects.

ties, indicating a uniform MoS<sub>2</sub> film. Fig. 4c shows an AFM image of the scratched MoS<sub>2</sub> film, revealing a flat surface with an ~0.6 nm-deep trench, confirming the formation of the SL MoS<sub>2</sub> film.

TEM analysis reveals the polycrystalline nature of the MoS<sub>2</sub> film. Fig. 4d shows a high-angle annular dark-field scanning transmission electron microscopy (HAADF-STEM) image of the transferred MoS<sub>2</sub> film. Upon closer examination, Moiré patterns<sup>35</sup> (indicated by the white arrows) are observed, suggesting twisted BL MoS<sub>2</sub> alongside the SL regions. The inset diffraction in Fig. 4d reveals five sets of hexagonal diffraction patterns corresponding to the 2H polymorph of MoS<sub>2</sub>. By masking other diffraction patterns and applying color-coding,<sup>22</sup> polycrystalline MoS<sub>2</sub> domains are revealed (Fig. 4e). This analysis shows that SL MoS<sub>2</sub> is the predominant layer, with minor BL and TL regions. Fig. 4f presents an HAADF-STEM image of grain boundaries between SL–SL regions, highlighting their atomic reconstruction with connected (6|4)–(7|5) defects, which are common in MoS<sub>2</sub>.<sup>52,53</sup>

#### Real-time growth kinetics of the continuous MoS<sub>2</sub> film

The growth kinetics leading to the continuous MoS<sub>2</sub> film were analyzed through a real-time growth video captured using an ICVDM.<sup>26</sup> To observe the growth kinetics, a MoS<sub>2</sub> film with a bare area was grown, while the bare area was generated using Denko tape (right panel of Fig. 4a). This sample provides contrast ( $C_R$ ) values of the growing layer<sup>26,34,54</sup> (see the Experimental section), and its growth trajectories were

recorded and are presented in the ESI (Video S1†). The video shows that the precursor spin-coat gradually transforms into a MoS<sub>2</sub> film without forming the typical triangular shape. This suggests that the growth occurs uniformly across the substrate, with crystallites smaller than the diffraction limit of the optical system (up to 660 nm, considering the numerical aperture (0.5) of the lens used in this experiment).

Fig. 5a shows the CVD programming profile, including the CVD temperature ( $T_{CVD}$ ), sulfur temperature ( $T_S$ ), and argon flow ( $F_{Ar}$ ) as a function of reaction time  $t_{rxn}$ . Real-time optical images corresponding to  $t_{rxn}$  are presented in Fig. 5b–d. At  $t_{rxn} = 30$  s (or  $T_{CVD} = 500$  °C), the spin-coat begins to change color, in which the precursor spin-coat area does not display a large contrast compared to the bare area. However, at  $t_{rxn} = 90$  s (or  $T_{CVD} = 600$  °C), the spin-coat rapidly changes color, with the interface showing a large contrast, indicating the formation of ML MoS<sub>2</sub>. At  $t_{rxn} = 4$  min (or  $T_{CVD} = 800$  °C), the film's color reaches saturation. Fig. 5e presents the  $C_R$  trends at various positions indicated in the optical images, depending on  $t_{rxn}$  and  $T_{CVD}$ . The deformation of the spin-coat starts at  $T_{CVD} = 500$  °C, consistent with a prior study.<sup>26</sup> Notably, unlike MoS<sub>2</sub> growth at 350 °C using volatile and fragile molybdenumhexacarbonyl (Mo(CO)<sub>6</sub>) and hydrogen sulfide (H<sub>2</sub>S) *via* metal-organic CVD,<sup>55</sup> the growth temperature for MoS<sub>2</sub> using Na<sub>2</sub>MoO<sub>4</sub> and sulfur as precursors can be reduced to as low as 500 °C. The  $C_R$  analysis<sup>26</sup> reveals that while position 1, located at the thick interface between the spin-coat and bare areas, forms ML MoS<sub>2</sub>, positions 2 and 3, which are farther from the



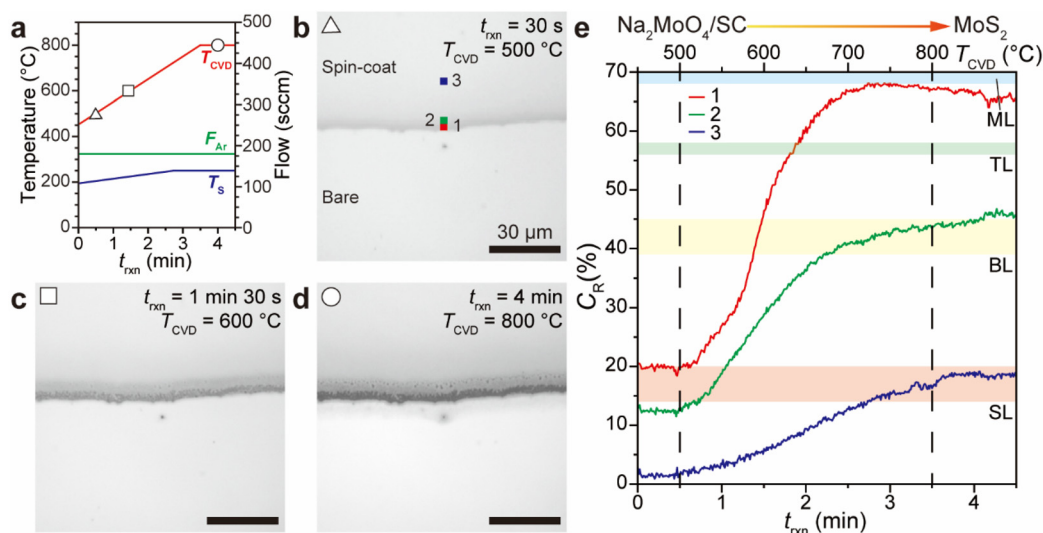


**Fig. 5** Growth kinetics of the continuous MoS<sub>2</sub> film observed using an ICVDM. (a) Programming parameter ( $T_{\text{CVD}}$ ,  $T_s$ , and  $F_{\text{Ar}}$ ) profiles during the ICVDM reaction. Real-time optical images of the MoS<sub>2</sub> film at  $t_{\text{rxn}} =$  (b) 30 s, (c) 1 min 30 s, and (d) 4 min. (e)  $C_R$  trends of the positions in the optical images in (b) according to  $t_{\text{rxn}}$  and  $T_{\text{CVD}}$ .

interface and therefore thinner, show BL and SL regions. The absence of intermediate triangular or hexagonal shapes in optical observation indicates that the MoS<sub>2</sub> film is composed of submicrometer-sized crystallites, which aligns with the TEM observations. Increasing the crystallite size would enhance the optoelectronic quality of the MoS<sub>2</sub> film, a topic for future investigation.

The catalytic roles of sodium and SC were explored through several control experiments. The first experiment used MoO<sub>3</sub> without SC, the second involved Na<sub>2</sub>MoO<sub>4</sub> without SC, and the third used MoO<sub>3</sub> with a different dispersant, such as SDS (see the Experimental section). The first experiment investigates the catalytic roles of sodium and SC, the second examines the role of SC, and the third explores the impact of SC's  $pK_a$ . Similar ICVDM experiments, as shown in Fig. S5a–S5g, S6a–S6g, and S7a–S7g† (see Note S3† for full details), were conducted. Briefly, MoO<sub>3</sub> spin-coating promotes MoS<sub>2</sub> growth at the interface between the spin-coat and bare areas at prolonged  $t_{\text{rxn}}$  (~10 min) at 800 °C (Fig. S5†). Na<sub>2</sub>MoO<sub>4</sub> only leads to the formation of discontinuous, micrometer-sized ML grains at extended  $t_{\text{rxn}}$  (~20 min) at 800 °C (Fig. S6†). Lastly, the MoO<sub>3</sub>/SDS case does not exhibit any MoS<sub>2</sub> features except for the interface after 10 min  $t_{\text{rxn}}$  at 800 °C (Fig. S7†). SDS, with a low  $pK_a$  (*i.e.*, 2), is ineffective in producing MoS<sub>2</sub>. From these experiments, the sodium catalyst from SC can lower the reaction temperature, and an appropriate  $pK_a$  value of the dispersant is an important aspect for continuous MoS<sub>2</sub> growth.

Thus far, we have shown that optimizing the pH of the metal precursor buffer facilitates the growth of continuous MoS<sub>2</sub> films. Additionally, we hypothesize that sodium content is another crucial factor influencing both the growth kinetics and the morphology of the films. Sodium particles that are optically visible promote the formation of ML MoS<sub>2</sub>, while

those that are optically invisible favor the growth of SL MoS<sub>2</sub>.<sup>26</sup> These sodium catalysts fragmented and moved along the edges, enhancing the MoS<sub>2</sub> growth.<sup>26,28</sup> Recent research indicates that sodium, decomposed from a Na<sub>2</sub>MoO<sub>4</sub> precursor, accumulates at the interface between MoS<sub>2</sub> and the SiO<sub>2</sub> substrate, becoming embedded into the substrate over extended growth periods.<sup>50</sup> This edge or interfacial sodium likely plays a significant role in influencing growth kinetics and morphology. Further investigation into this process will be an important direction for future research.

## Conclusions

In this study, we achieved continuous, centimeter-scale MoS<sub>2</sub> growth on a SiO<sub>2</sub> surface using an SC-buffered, uniformly spin-coatable metal precursor *via* the CVD process. This method leverages a sodium molybdate/SC complex with  $pH = 5.3$ , based on the  $pK_a$  values of the metal precursor, dispersant, and substrate. By systematically exploring sodium-based metal precursor dispersions, we presented a reproducible relationship between the precursor concentration and the number of MoS<sub>2</sub> layers. By minimizing moisture exposure, we achieved robust, reproducible MoS<sub>2</sub> growth with randomly oriented polycrystallites. Our findings demonstrate that the increased adsorbed concentration of metal precursors directly influences the increasing number of MoS<sub>2</sub> layers, providing precise control over the resulting structures. These mildly acidic metal precursor dispersions support patterned continuous growth and are compatible with photolithography techniques for further device integration. An ICVDM allows us to observe the growth kinetics of continuous MoS<sub>2</sub> according to the reaction time and furnace temperature, indicating that the growth



occurs even at temperatures as low as 500 °C. Several control experiments investigating the roles of sodium, SC, and the  $pK_a$  of SC further highlight the critical importance of the *in situ* formation of  $\text{Na}_2\text{MoO}_4$  facilitated by SC. This simple spin-coating method provides a route to produce complex hierarchical TMC structures with high reproducibility, advancing the development of optoelectronic devices.

## Author contributions

D. H. Kim performed the experiments, characterized the samples, and analyzed the data. J. Seo and Y. Kang performed the experiments. B. Lee performed the experiments and analyzed the data. S.-Y. Ju conceived the idea and supervised the project. S.-Y. Ju wrote the manuscript. All the images/artwork/photos that appear in the manuscript and ESI† were created by the authors of this manuscript.

## Data availability

The data supporting this article have been included as part of the ESI.†

## Conflicts of interest

We have filed a Korean Patent (filing date: 2024.11.19, filing number: 10-2024-0165414) regarding pH-optimized metal precursor dispersion for CVD growth of TMCs.

## Acknowledgements

This research was supported financially by YU-KRISS (KRISS-GP2024-0012-GONG9), and in part by the Basic Science Research Program (NRF-2022R1A2C1006932) through the National Research Foundation of Korea (NRF) funded by the Ministry of Education, Science, and Technology.

## References

- A. Splendiani, L. Sun, Y. Zhang, T. Li, J. Kim, C.-Y. Chim, G. Galli and F. Wang, *Nano Lett.*, 2010, **10**, 1271–1275.
- B. Radisavljevic, A. Radenovic, J. Brivio, V. Giacometti and A. Kis, *Nat. Nanotechnol.*, 2011, **6**, 147–150.
- Y.-H. Lee, L. Yu, H. Wang, W. Fang, X. Ling, Y. Shi, *et al.*, *Nano Lett.*, 2013, **13**, 1852–1857.
- A. Castellanos-Gomez, M. Buscema, R. Molenaar, V. Singh, L. Janssen, H. S. J. van der Zant and G. A. Steele, *2D Mater.*, 2014, **1**, 011002.
- P. Rivera, K. L. Seyler, H. Yu, J. R. Schaibley, J. Yan, D. G. Mandrus, W. Yao and X. Xu, *Science*, 2016, **351**, 688–691.
- K. Kang, K.-H. Lee, Y. Han, H. Gao, S. Xie, D. A. Muller and J. Park, *Nature*, 2017, **550**, 229–233.
- Y. Meng, T. Wang, C. Jin, Z. Li, S. Miao, Z. Lian, *et al.*, *Nat. Commun.*, 2020, **11**, 2640.
- R. Rosati, I. Paradisanos, L. Huang, Z. Gan, A. George, K. Watanabe, *et al.*, *Nat. Commun.*, 2023, **14**, 2438.
- Z. Yin, H. Li, H. Li, L. Jiang, Y. Shi, Y. Sun, *et al.*, *ACS Nano*, 2012, **6**, 74–80.
- J. S. Kim, H. S. Lee, P. J. Jeon, Y. T. Lee, W. Yoon, S.-Y. Ju and S. Im, *Small*, 2014, **10**, 4845–4850.
- V. K. Kumar, S. Rathkanthiwar, A. Rao, P. Ghosh, S. Dhar, H. Chandrasekar, T. Choudhury, S. A. Shivashankar and S. Raghavan, *ACS Appl. Nano Mater.*, 2021, **4**, 6734–6744.
- H. Choi, B. H. Moon, J. H. Kim, S. J. Yun, G. H. Han, S.-g. Lee, H. Z. Gul and Y. H. Lee, *ACS Nano*, 2019, **13**, 13169–13175.
- Z. Y. Zhu, Y. C. Cheng and U. Schwingenschlöggl, *Phys. Rev. B: Condens. Matter Mater. Phys.*, 2011, **84**, 153402.
- K. F. Mak, K. He, J. Shan and T. F. Heinz, *Nat. Nanotechnol.*, 2012, **7**, 494–498.
- K. F. Mak, K. L. McGill, J. Park and P. L. McEuen, *Science*, 2014, **344**, 1489–1492.
- H. Yuan, X. Wang, B. Lian, H. Zhang, X. Fang, B. Shen, *et al.*, *Nat. Nanotechnol.*, 2014, **9**, 851–857.
- N. Zibouche, P. Philipsen, A. Kuc and T. Heine, *Phys. Rev. B: Condens. Matter Mater. Phys.*, 2014, **90**, 125440.
- Z. Li, X. Meng and Z. Zhang, *J. Photochem. Photobiol., C*, 2018, **35**, 39–55.
- Y. Luo, K. Ren, S. Wang, J.-P. Chou, J. Yu, Z. Sun and M. Sun, *J. Phys. Chem. C*, 2019, **123**, 22742–22751.
- A. M. van der Zande, P. Y. Huang, D. A. Chenet, T. C. Berkelbach, Y. You, G.-H. Lee, *et al.*, *Nat. Mater.*, 2013, **12**, 554–561.
- S. Wang, Y. Rong, Y. Fan, M. Pacios, H. Bhaskaran, K. He and J. H. Warner, *Chem. Mater.*, 2014, **26**, 6371–6379.
- K. Kang, S. Xie, L. Huang, Y. Han, P. Y. Huang, K. F. Mak, C.-J. Kim, D. Muller and J. Park, *Nature*, 2015, **520**, 656–660.
- G. H. Han, N. J. Kybert, C. H. Naylor, B. S. Lee, J. Ping, J. H. Park, *et al.*, *Nat. Commun.*, 2015, **6**, 6128.
- S. Li, Y.-C. Lin, W. Zhao, J. Wu, Z. Wang, Z. Hu, *et al.*, *Nat. Mater.*, 2018, **17**, 535–542.
- S. Li, Y.-C. Lin, X.-Y. Liu, Z. Hu, J. Wu, H. Nakajima, *et al.*, *Nanoscale*, 2019, **11**, 16122–16129.
- J. Oh, M. Park, Y. Kang and S.-Y. Ju, *ACS Nano*, 2024, **18**, 19314–19323.
- J. Zhou, J. Lin, X. Huang, Y. Zhou, Y. Chen, J. Xia, *et al.*, *Nature*, 2018, **556**, 355–359.
- L. Huang, Q. H. Thi, F. Zheng, X. Chen, Y. W. Chu, C.-S. Lee, J. Zhao and T. H. Ly, *J. Am. Chem. Soc.*, 2020, **142**, 13130–13135.
- H. Wang, X. Zhu, Z. Zhao, X. Wang, Z. Qian, L. Jiao, *et al.*, *Nano Lett.*, 2024, **24**, 5498–5505.
- E. Koo, Y. Lee, Y. Song, M. Park and S.-Y. Ju, *ACS Appl. Electron. Mater.*, 2019, **1**, 113–121.



- 31 Y. Song, M. Park, J. Park, H. S. Ahn, T. K. Kim and S.-Y. Ju, *Nanomaterials*, 2022, **12**, 1706.
- 32 J. Park, S. Bong, J. Park, E. Lee and S.-Y. Ju, *ACS Appl. Mater. Interfaces*, 2022, **14**, 50308–50317.
- 33 S. Hong, M. Park, S. Kwon, J. Oh, S. Bong, B. Krishnakumar and S.-Y. Ju, *Carbon*, 2021, **183**, 84–92.
- 34 E. Koo and S.-Y. Ju, *Carbon*, 2015, **86**, 318–324.
- 35 E. Koo, S. Kim and S.-Y. Ju, *Carbon*, 2017, **111**, 238–247.
- 36 J. Park, Y. R. Han, M. Park, C.-H. Jun and S.-Y. Ju, *Carbon*, 2020, **161**, 599–611.
- 37 M. Jeong, S. Kim and S.-Y. Ju, *RSC Adv.*, 2016, **6**, 36248–36255.
- 38 L. Chen, X. He, H. Liu, L. Qian and S. H. Kim, *J. Phys. Chem. C*, 2018, **122**, 11385–11391.
- 39 S. Bong, S. Hwang and S.-Y. Ju, *J. Phys. Chem. C*, 2024, **128**, 11229–11238.
- 40 Technical Data Sheet: Sodium Molybdate Dihydrate, <https://northmetal.net/wp-content/uploads/Sodium-Molybdate-Dihydrate-Sodium-Molybdate-SMX-Na2MoO4-H2O-NaMoO4-10102-40-6-TDS-2.pdf>, accessed 2025.03.20.
- 41 D. J. Belton, O. Deschaume and C. C. Perry, *FEBS J.*, 2012, **279**, 1710–1720.
- 42 S. Asbrink, L. Kihlberg and M. Malinowski, *J. Appl. Crystallogr.*, 1988, **21**, 960–962.
- 43 T. P. Dadze, G. A. Kashirtseva, M. P. Novikov and A. V. Plyasunov, *Fluid Phase Equilib.*, 2017, **440**, 64–76.
- 44 W. L. Lindsay and K. M. Catlett, in *Future Prospects for Soil Chemistry*, ed. P. M. Huang, 1998, pp. 123–138.
- 45 J. J. Cruywagen, in *Advances in Inorganic Chemistry*, ed. A. G. Sykes, Academic Press, 1999, vol. 49, pp. 127–182.
- 46 Z. Minubayeva and T. M. Seward, *Geochim. Cosmochim. Acta*, 2010, **74**, 4365–4374.
- 47 D. J. Cabral, J. A. Hamilton and D. M. Small, *J. Lipid Res.*, 1987, **27**, 334–343.
- 48 R. K. Rana and B. Viswanathan, *Catal. Lett.*, 1998, **52**, 25–29.
- 49 O. G. Abdullah, S. B. Aziz, D. R. Saber, R. M. Abdullah, R. R. Hanna and S. R. Saeed, *J. Mater. Sci.: Mater. Electron.*, 2017, **28**, 8928–8936.
- 50 R. A. Kalt, A. Arcifa, C. Wäckerlin and A. Stemmer, *Nanoscale*, 2023, **15**, 18871–18882.
- 51 C. Lee, H. Yan, L. E. Brus, T. F. Heinz, J. Hone and S. Ryu, *ACS Nano*, 2010, **4**, 2695–2700.
- 52 W. Zhou, X. Zou, S. Najmaei, Z. Liu, Y. Shi, J. Kong, *et al.*, *Nano Lett.*, 2013, **13**, 2615–2622.
- 53 N. Gao, Y. Guo, S. Zhou, Y. Bai and J. Zhao, *J. Phys. Chem. C*, 2017, **121**, 12261–12269.
- 54 H. Zhang, Y. Ma, Y. Wan, X. Rong, Z. Xie, W. Wang and L. Dai, *Sci. Rep.*, 2015, **5**, 8440.
- 55 J. Mun, Y. Kim, I.-S. Kang, S. K. Lim, S. J. Lee, J. W. Kim, H. M. Park, T. Kim and S.-W. Kang, *Sci. Rep.*, 2016, **6**, 21854.

